Journal of Materials Chemistry B

PAPER

View Article Online
View Journal | View Issue

Published on 05 September 2014. Downloaded by Oregon State University on 6/23/2023 8:02:32 PM.

Cite this: J. Mater. Chem. B, 2014, 2, 6867

Fabrication and evaluation of electrospun PCL–gelatin micro-/nanofiber membranes for anti-infective GTR implants†

Jiajia Xue,[a] Min He,[a] Yuanzhe Liang,[a] Aileen Crawford,[b] Phil Coates,[c] Dafu Chen,[d] Rui Shi*[d] and Liqun Zhang*[a]

Received 8th May 2014
Accepted 21st June 2014

DOI: 10.1039/c4tb00737a

www.rsc.org/MaterialsB

Infection is the major reason for GTR/GBR membrane failure in clinical applications. In this work, we developed GTR/GBR membranes with localized drug delivery function to prevent infection. Hierarchical membranes containing micro- and nano-fibers were fabricated. The effects of the incorporation of gelatin and loading content of metronidazole (MNA) (0, 5, 10, 20, 30, and 40 wt% polymer) on the properties of the electrospun membranes were investigated. The interaction between PCL and MNA was identified by molecular dynamics simulation. MNA was released in a controlled manner, and the antibacterial activity of the released MNA remained. The incorporation of gelatin and MNA improved the hydrophilicity, biocompatibility, and *in vitro* biodegradation rate of PCL nanofibers. The electrospun membranes allowed cells to adhere to and proliferate on them and showed excellent barrier function. The membrane loaded with 30% MNA had the best comprehensive properties. Subcutaneous implantation results demonstrated that MNA-loaded membranes evoked a less severe inflammatory response than pure PCL nanofibers. These results demonstrated the potential of MNA-loaded membranes as GTR/GBR membranes with antibacterial and anti-inflammatory functions for biomedical applications.

1 Introduction

Guided tissue regeneration/guided bone regeneration (GTR/GBR) technologies have become a standard procedure for tissue and bone regeneration therapy.[1] GTR/GBR membranes, which are used not only to perform the barrier function by preventing the ingrowth of fibroblast cells into the tissue/bone defect site but also to improve the tissue/bone regeneration by supporting cells to attach and proliferate, need to have biocompatibility, proper degradation profile, and adequate mechanical and physical properties.[2]

Infection is currently considered as the major reason for GTR/GBR failure in clinical applications, constituting a significant healthcare burden.[3] Infection resistant GTR/GBR membranes have attracted more and more attention.[4] Infection is caused by either bacterial colonization at the wound site or foreign body response resulting from the implant material.[5] Antibacterial biomaterials are one of the greatest interests in the war against implant-related infections, representing the broadest group of anti-infective biomaterials.[6,7] Focal antibacterial drug-loaded biomaterials can deliver a desired drug dose directly to the infected site for an extended time period while minimizing systemic distribution of toxic drugs.[8,9] Our purpose is to develop an anti-infective GTR/GBR membrane with localized antibacterial drug release function.

Electrospinning has gained widespread interest in tissue engineering and drug delivery because of its relative ease of use and adaptability. The structure of inherently high surface to volume ratio electrospun polymer fibers can improve cell attachment, enhance drug loading, and realize sustained and controlled local drug delivery.[10] A broad range of biomolecules have been successfully encapsulated in polymer nanofibers through electrospinning while the bioactivity of the biomolecules remains.[11,12] The drug release profile and the degradation rate of the electrospun membranes can be adjusted by tailoring the parameters during the electrospinning process.[13,14] Therefore, the electrospinning process was adopted to fabricate the antibacterial membranes in this study.

Numerous natural and synthetic polymers have been investigated for the fabrication of GTR/GBR membranes. Collagen has excellent biocompatibility, but it collapses quickly during

[a]Beijing Laboratory of Biomedical Materials, Beijing University of Chemical Technology, Beijing 100029, PR China. E-mail: zhanglq@mail.buct.edu.cn; Fax: +86 10 64433964; Tel: +86 10 64421186

[b]Centre for Biomaterials and Tissue Engineering, University of Sheffield, Sheffield, South Yorkshire S3 7HQ, UK

[c]School of Engineering, Design & Technology, University of Bradford, Bradford, West Yorkshire BD7 1DP, UK

[d]Laboratory of Bone Tissue Engineering of Beijing Research Institute of Traumatology and Orthopaedics, Beijing 100035, China. E-mail: sharell@126.com

† Electronic supplementary information (ESI) available. See DOI: 10.1039/c4tb00737a

Published on 05 September 2014. Downloaded by Oregon State University on 6/23/2023 8:02:32 PM.

the degradation process.[15] Although PLA- and PLGA-based nanofiber membranes are also biocompatible and biodegradable, the rapid releases of oligomers and acid by-products during degradation may cause significant inflammation reactions and foreign body response *in vivo*.[16] PCL is extensively studied for controlled drug delivery and tissue engineering applications.[17] Its compatibility with a wide range of drugs enables uniform drug distribution in the matrix.[18] PCL has good mechanical properties, but its low hydrophilicity together with a lack of functional groups often results in low cell adhesion and proliferation. The biodegradation rate of PCL is low. Gelatin, a natural biopolymer derived from partial hydrolysis of native collagen, has many integrin-binding sites for cell adhesion and differentiation.[19] A PCL–gelatin hybrid material, a new biomaterial with good biocompatibility and improved mechanical, physical, and chemical properties,[20] has been successfully applied in cartilage regeneration,[21,22] nerve engineering, wound dressing,[23] cardiac tissue engineering,[24] muscle tissue engineering,[25] and other tissue engineering potential applications.[26,27]

Periodontal disease and infection associated with GTR/GBR implants result mainly from anaerobic bacteria. Metronidazole (MNA) has been successfully used for the treatment of anaerobic bacterial infections for more than 45 years.[28] MNA was integrated into polylactic nanofibers for local periodontitis treatment, and the drug delivery system showed sustained drug release properties and significantly decreased the viability of bacteria.[29] An MNA-loaded PLGA (poly(lactic-*co*-glycolic acid)) membrane fabricated by solvent casting showed a significant improvement on the periodontal regeneration following GTR in dogs.[30] Thus, MNA-loaded PCL–gelatin was electrospun to obtain anti-infective GTR/GBR membranes in this study.

The effects of MNA content in a wide range (0–40 wt%) and gelatin on the properties of the membranes were studied. The interaction between the drug and polymer matrix was investigated through a series of analyses including molecular dynamics simulation. Particularly, an *in vitro* method was designed to evaluate the barrier function of the membrane to fibroblast cells; the method was proved as an effective way to predict the *in vivo* barrier function of membranes. With this method, animal experiments could be avoided. A membrane with the optimum drug loading content for anti-infection effects and comprehensive properties except cytotoxicity was obtained. A long term subcutaneous implantation of the obtained drug-loaded membrane showed good anti-infection properties and biocompatibility. The current work is expected to provide valuable information for the development of GTR/GBR membranes.

2 Materials and methods

2.1 Preparation of electrospun membranes

The materials used in this study are listed in S1.† PCL was dissolved in a DCM : DMF (60 : 40 v/v) mixture at a concentration of 10 wt%. MNA at a concentration of 30 wt% of PCL was added to the solution. The PCL nanofiber membrane was labeled as P0, and the PCL membrane with 30 wt% MNA was labeled as P30. A solution of PCL–gelatin was made by mixing 6 wt% PCL/TFE and 6 wt% gelatin/TFE in the mass ratio of 50 : 50. MNA, in the range of 1–40% w/w of the polymer used, was added to the PCL–gelatin solution. The solution was fed at a rate of 1 mL h^{-1} by a syringe pump to the needle tip of a 20 mL syringe with a needle diameter of 0.4 mm. Optimized high voltage (8–12 kV) was applied between the needle and the grounded collector, which was laid with aluminum foil at a rotating rate of 300 rpm. The needle was located at a distance of 20 cm from the ground collector. The membranes fabricated from the PCL solution is labeled as P0, and the membranes fabricated from the PCL–gelatin solution with MNA contents of 0%, 5%, 10%, 20%, 30%, and 40% were labeled as PG0, PG5, PG10, PG20, PG30, and PG40, respectively.

2.2 Characterization of PG–MNA membranes

2.2.1 Morphology of PG–MNA membranes. The morphology of the membranes was observed by scanning electron microscopy (SEM). The membranes were coated with gold before being observed under the microscope (S4800, Hitachi, Japan) at a voltage of 5 kV. The fiber diameter and pore size were measured by using the Image J software on SEM micrographs at 100 random locations. The thickness of a membrane was measured with a micrometer. The apparent density and porosity of the membrane were estimated by using eqn (1) and (2), respectively:[23]

$$\text{Apparent density}\left(\text{g cm}^{-3}\right) = \frac{\text{mass of membrane(g)}}{\text{membrane thickness(cm)} \times \text{membrane area(cm}^2\text{)}}, \quad (1)$$

$$\text{Porosity}(\%) = \left(1 - \frac{\text{apparent density(g cm}^{-3}\text{)}}{\text{bulk density(g cm}^{-3}\text{)}}\right) \times 100\%, \quad (2)$$

2.2.2 Molecular dynamics simulation, and chemical, thermal, and mechanical analyses of PG–MNA membranes. For the molecular dynamics simulation, the Discover and Amorphous Cell modules of the Materials Studio suite were used. All the theoretical calculations were performed by using the condensed-phase optimized molecular potentials for atomistic simulation studies (COMPASS) force field (see S2†). FTIR, DSC, and X-ray diffraction (XRD) analyses were performed to investigate the chemical and thermal properties of the membranes. The mechanical properties were evaluated by tensile tests (see S3†).

2.2.3 Apparent water contact angle (WCA) measurements. The static WCAs of all membranes were measured using an SL200A type Contact Angle Analyzer (Solon (Shanghai) Technology Science Co., Ltd., China) at ambient temperature. Water droplets (3.0 μL) were dropped carefully onto the surface of the electrospun membranes. The average WCA value was obtained by measuring ten water droplets at randomly distributed positions.

2.2.4 Drug encapsulation efficiency and drug release profile. The drug encapsulation efficiency of a MNA-loaded membrane was determined as follows. A known mass of

 This journal is © The Royal Society of Chemistry 2014

Published on 05 September 2014. Downloaded by Oregon State University on 6/23/2023 8:02:32 PM.

membrane was dissolved in 1 mL of TFE, and the solution was added dropwise to 20 mL of methanol, in which the polymer was precipitated and MNA was dissolved. After centrifugation of the methanol solution, the liquid supernatant was detected by HPLC at $\lambda_{max} = 310$ nm. The amount of MNA was obtained from the calibration curve of MNA. The encapsulation efficiency was calculated by the following equation:

$$\text{Encapsulation efficiency } \% = \frac{\text{weight of drug in the sample(g)}}{\text{theoretical weight of drug in the sample(g)}} \times 100\%. \quad (3)$$

The drug release profile of a MNA-loaded membrane was determined by soaking the membrane in triplicate in phosphate buffered saline (PBS, pH = 7.4). The membrane was cut into circles 2 cm in diameter, accurately weighed and incubated in 5 mL of PBS at 37 °C with mild shaking. At pre-determined time intervals, 1 mL of soaking solution was collected for HPLC detection to determine the amount of drug released. The remaining medium was removed and replaced with another 5 mL of fresh PBS to maintain the sink condition where saturation solubility of a drug in the dissolution medium is at least three times more than the drug concentration.[31] Only if the sink condition was maintained, the drug release profile was realistic. The percentage of the drug released was calculated based on the initial weight of the drug incorporated into the electrospun membrane.[13]

2.2.5 *In vitro* biodegradation of PG-MNA membranes. The membranes were cut into circular samples 2 cm in diameter, weighed, and soaked in 5 mL of PBS in 12-well plates at 37 °C. The sample weights were plotted against time to obtain the degradation profile of the membranes. The morphology and tensile properties of the membranes during degradation were measured by SEM and tensile testing, respectively.

2.3 Biocompatibility, barrier function and antibacterial activity

2.3.1 Biocompatibility. The cytotoxicity of the membranes to L929 fibroblast cells, human periodontal ligament fibroblasts (hPDLFs), and rat osteogenesis sample (ROS) cells was evaluated (see S4†). Cell Counting Kit-8 (CCK-8) assay was used to test the attachment and proliferation of L929 fibroblast cells on the membranes (see S5†). The proliferation of hPDLFs and ROS cells on the PG30 membrane was also tested by using PrestoBlue assay (Life Technologies) as described in S5.†

2.3.2 Barrier function to fibroblast cells. The *in vitro* barrier function of the membranes to L929 cells as model cells was evaluated by our design (details in S6†) to determine whether cells got through the membranes. The barrier function of the membranes after 1 month of degradation in PBS was also evaluated.

2.3.3 *In vitro* antibacterial activity. The antibacterial activity of the membranes against the typical anaerobic bacteria *Fusobacterium nucleatum* (ATCC 25586, Chinese General Microbiological Culture Collection Center), which is commonly found in the oral cavity in an infection, was determined by the modified Kirby–Bauer method, as previously described.[32] A 100 μL aliquot of *Fusobacterium nucleatum* reconstituted in Brian Heart Infusion culture medium and previously subcultured was spread onto an agar plate. Sections (1.0 cm × 1.0 cm) of a membrane in triplicate were placed on the plate and incubated for different times at 37 °C under anaerobic conditions. The bacterial growth on the plate was visualized directly and the diameter of the inhibition zone was measured on days 1, 4, 7, 14, 21, and 30.

2.4 *In vivo* biocompatibility and degradation of the PG–MNA membrane

In vitro results revealed that PG30 had the best *in vitro* biocompatibility, the highest antibacterial ability, and the best comprehensive properties to meet the required specifications for the GTR membrane. Therefore, PG30 was selected to assess the *in vivo* anti-infection property, biocompatibility and biodegradability compared with P0 and P30.

2.4.1 Subcutaneous implantation. Forty healthy adult male New Zealand white rabbits (2.5–3.0 kg each) were used as experimental animals. The protocol for animal experiments was approved by the Animal Ethical Committee of the Laboratory of Bone Tissue Engineering of Beijing Research Institute of Traumatology and Orthopedics, and national guidelines for the care and use of laboratory animals were applied. Based on *in vitro* data, P0, P30 and PG30 were used for the *in vivo* evaluation. Samples (1.5 cm × 1.5 cm) were sterilized by γ-irradiation. The animals were anesthetized with isoflurane, and their backs were shaved and sterilized with alcohol and iodine scrubs. Three paravertebral incisions (2 cm each) per rabbit were made approximately 1 cm lateral to the vertebral column to expose the dorsal subcutis. Subcutaneous pockets were created by blunt dissection. Each individual pocket held one membrane, and the incisions were closed with surgical sutures. All surgeries were carried out in an aseptic field by using an aseptic technique. A total of 32 samples (four averages at each implantation time point) for each of the three membranes were implanted.

2.4.2 Gross morphology and histology. The long term biocompatibility and the effect of the degradation by-products on the tissue of the samples were evaluated for 8 months of implantation. After post-surgery 1 week, 3 weeks, 5 weeks, 7 weeks, 8 weeks, 3 months, 6 months, and 8 months, the implants were harvested for examination. The harvested implants were fixed in 10% formalin solution overnight and then dehydrated in a graded series of ethanol. Explants were embedded in paraffin and cut into 6 μm sections in a transverse direction by using a standard microtome. The sections were cut from at least three arbitrary regions perpendicular to the long axis of the tissue capsule and stained with hematoxylin and eosin (H&E) for morphological evaluation. The infiltration of inflammatory cells was assessed by comparing the number of neutrophils, macrophages, and foreign body giant cells surrounding the tissue of the implant to evaluate the extent of acute inflammation, chronic inflammation, granulation tissue development, and foreign body reaction after 1 week and 3 weeks post-surgery. A high infiltrating cell density was taken as

Published on 05 September 2014. Downloaded by Oregon State University on 6/23/2023 8:02:32 PM.

an indication of poor biocompatibility. After the samples had been implanted for 3 weeks, the biocompatibility of each sample was assessed by checking the thickness of the inflammatory fibrous capsule formed around a cross-section of the implant. A thick capsule was taken as an indication of poor biocompatibility.[33,34]

2.4.3 SEM observation. Explanted membranes used for SEM studies were washed three times with Dulbecco's phosphate buffered saline (D-PBS; PBS without Ca^{2+} or Mg^{2+}, pH 7.2) and fixed in 3% glutaraldehyde overnight prior to dehydration in a graded series of ethanol (30%, 50%, 70%, 90%, 95% and 100%, 1 h each). Then the samples were left to dry in air in a fume hood for 1 h. The completely dried samples were sputter-coated with gold and observed by SEM.

2.5 Statistical analysis

Statistical comparisons for significance were conducted using Students' *t*-test with a 95% confidence level. Each data point was expressed as mean ± standard deviation.

3 Results and discussion

3.1 Characterization of PG–MNA membranes

3.1.1 Morphology of PG–MNA membranes. The SEM micrographs of the membranes are shown in Fig. 1. The micrograph images show a randomly interconnected structure with no beads formed, and a distribution of micro- and nanofibers in the membranes. The formation of microfibers and nanofibers simultaneously in the membranes may be the result of the immiscibility and phase separation of PCL and gelatin in the electrospinning solution. The pH of the electrospinning solution is close to the pH of gelatin's isoelectric point, at which gelatin tends to aggregate, resulting in phase separation. Gelatin is a polyelectrolyte polymer with many ionizable groups such as amino and carboxylic groups and can produce ions soluble in the solvent.[35] The electrical conductivity of PG electrospinning solution increases with the addition of gelatin, but the diameter of fibers decreases with the increase of electrical conductivity of electrospinning solution.[36] As a result, under the same electrospinning conditions, the diameter of fibers with gelatin ionic molecules is smaller than that of fibers with PCL non-ionic molecules. Thus, the PG–MNA membranes contain gelatin nanofibers and PCL microfibers, as confirmed by the SEM micrographs of the fibers after gelatin degradation. This micro- and nanofiber hybrid may result in different cell behaviors on the membrane.[38] As shown in Table 1, the diameters of the microfibers with different contents of drug are in the range of 1.51–2.67 μm while the diameters of the nanofibers are in the range of 280–470 nm. The content of MNA incorporated into the fibers affects the fiber diameter.

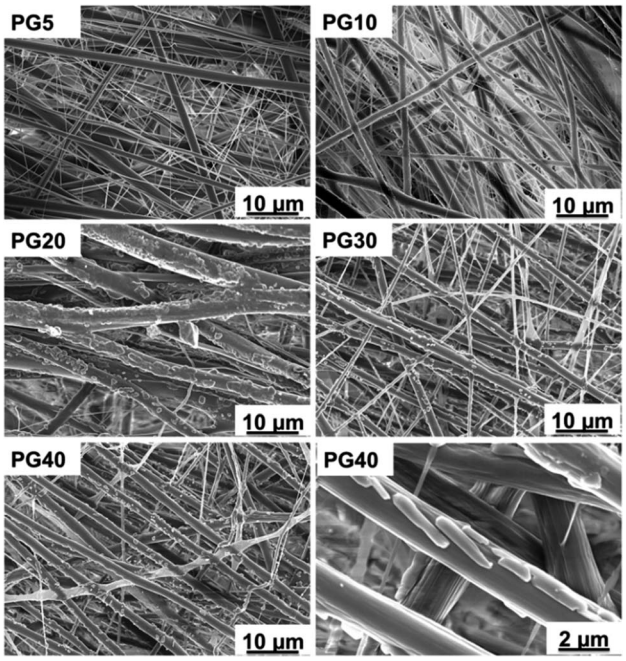

Fig. 1 SEM micrographs of electrospun membranes with different contents of MNA.

The SEM micrographs in Fig. 1 show that the surface of the fibers in PG5 and PG10 are smooth, but there are nanocrystals on the surface of the fibers in PG20, PG30 and PG40. MNA can form strong intermolecular interactions with gelatin, which is hydrophilic, and strong hydrogen bonds with PCL (S7†). At MNA content lower than 20%, the MNA molecules are dispersed in the polymer at the molecular level. But as the MNA content increases to over 20%, the MNA molecules tend to aggregate to form nanocrystals. Because the interaction between MNA and gelatin is stronger than that between MNA and PCL, the MNA molecules are dispersed more evenly in gelatin than in PCL. Thus, more MNA crystals are observed on the surface of PCL microfibers than on the surface of gelatin nanofibers.

The much smaller pore sizes of the membranes than the size of fibroblasts are beneficial to prevent the ingrowth of fibroblasts into the tissue defects. The porosities of the membranes are all in the range of 60–80%, ensuring sufficient gas and nutrient exchanges.

3.1.2 Chemical, thermal, and mechanical properties of PG–MNA membranes. According to the ATR-FTIR spectra of the electrospun membranes (Fig. 2(a)), the PCL-related stretching

Table 1 Fiber diameter, pore size and porosity of electrospun membranes with different contents of MNA

Sample	MNA (wt%)	Fiber diameter (μm)	Pore size (μm)	Porosity (%)
PG5	5	1.99 ± 0.30 0.28 ± 0.10	4.73 ± 0.80	71.6
PG10	10	1.87 ± 0.40 0.32 ± 0.10	4.06 ± 0.70	72.3
PG20	20	2.67 ± 0.50 0.47 ± 0.10	5.35 ± 1.20	69.7
PG30	30	1.51 ± 0.30 0.30 ± 0.10	3.21 ± 0.80	70.5
PG40	40	1.87 ± 0.20 0.44 ± 0.10	3.92 ± 0.70	72.6

This journal is © The Royal Society of Chemistry 2014

Published on 05 September 2014. Downloaded by Oregon State University on 6/23/2023 8:02:32 PM.

modes are presented by the peaks at 2943 cm^{-1} (asymmetric CH_2 stretching), 2866 cm^{-1} (symmetric CH_2 stretching), 1721 cm^{-1} (C=O stretching), 1294 cm^{-1} (C–O and C–C stretching), and 1240 cm^{-1} (asymmetric C–O–C stretching). Several characteristic peaks of gelatin appear at approximately 1650 cm^{-1} (amide I) and 1540 cm^{-1} (amide II), corresponding to the stretching vibrations of the C=O bond, and the coupling of bending of the N–H bond and stretching of C–N bonds, respectively.[37] The MNA-related stretching modes are represented by the peaks at 3414 cm^{-1} and 3220 cm^{-1} (O–H stretching), 3097 cm^{-1} (=CH stretching), and 1550 cm^{-1} ($-NO_2$ antisymmetric stretching). The characteristic peaks of the MNA encapsulated in the membranes are no different from those of pure MNA crystals, and the relative intensity of these peaks increases with increasing MNA content. Besides, the peak widths of the characteristic hydroxyl bands of MNA at 3414 cm^{-1} and 3220 cm^{-1} increase because of the hydrogen interaction between MNA and the polymer matrix. There are also interactions like hydrogen interaction between PCL and gelatin.[25] The hydrogen bonds between MNA, PCL and gelatin are beneficial to the dispersion and controlled release of MNA. The electrospinning process does not adversely affect the molecular structure of MNA, especially the antibacterial $-NO_2$ group.

From the DSC thermograms shown in Fig. 2(b), at MNA contents lower than 20 wt%, the absence of the MNA melting peak indicates that MNA is dispersed on the molecular level. At MNA contents of 20 wt%, 30 wt%, and 40 wt%, the melting peak of MNA appears, indicating the formation of MNA crystals. For drug-loaded biomedical materials, the drug should be stable in the polymer matrix during the storage period. The DSC thermograms of the membranes after storage for 1 month, 3 months, and 6 months (data not shown) showed that the thermal properties of the membranes did not change with storage time.

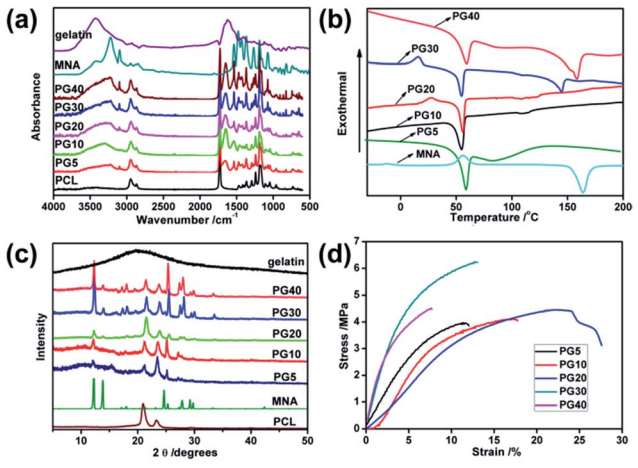

Fig. 2 Chemical, thermal, and mechanical properties of the electrospun membranes with different contents of MNA: (a) FTIR spectra, (b) DSC thermograms, (c) XRD patterns, and (d) stress–strain curves in the wet state.

In the XRD pattern of PCL (Fig. 2(c)), the two diffraction peaks located at 21.4° and 23.8° are assigned to semi-crystalline PCL. The absence of a diffraction peak in the XRD pattern of gelatin shows that gelatin is amorphous. As the MNA content increases, the two peaks of PCL shift to slightly higher angles, indicating that the length of PCL crystal stacks decrease, probably because the MNA molecules and gelatin molecular chains among the PCL molecular chains restrain the formation of PCL crystal stacks. The orientation of the PCL molecular chains during the electrospinning process also affects the PCL crystallization. As the MNA content increases to over 10%, the characteristic diffraction peaks of MNA located at 12.2° and 13.8° appear, which demonstrate the aggregation of MNA.

Since MNA is highly soluble in the solvent for electrospinning and the MNA molecules can form hydrogen bonds with the polymer matrix, no MNA molecules precipitate from the electrospinning solution during the electrospinning process. Thus, at low drug contents, MNA is well dispersed inside the fibers. However, at MNA contents higher than 20%, some MNA molecules form hydrogen bonds with other MNA molecules, and weak aggregation of MNA occurs in the fibers, leading to the appearance of a melting peak in the DSC curve and crystalline peaks in the XRD pattern, in accordance with the SEM observations of MNA crystals on the surface of the fibers.

For bone/tissue regeneration, the porous membrane must be strong enough to withstand the forces during surgical operation and those exerted by physiological activities and/or by tissue growth. The stress–strain curves in Fig. 2(d) show that the membranes are elastic, a property critical for GTR membranes. The tensile strengths of the membranes in the wet state are in the range of 3.97–6.23 MPa, which meet the clinical GTR requirements. With the increase of MNA content, the tensile strength first increases, reaches a maximum at an MNA content of 30% (PG30), and then decreases.

3.1.3 Apparent WCA of PG–MNA membranes. The hydrophilicity of biomaterials has great influence on the adhesion and proliferation of cells. The PCL electrospun nanofiber membrane is moderately hydrophobic, with a contact angle of 129.6° (Fig. 3). The incorporation of gelatin significantly increases the hydrophilicity of PG–MNA membranes because of the amine and carboxyl functional groups in gelatin. Besides, with the increase of MNA content, the contact angle of the PG–MNA membranes decreases because of the hydroxyl and polar

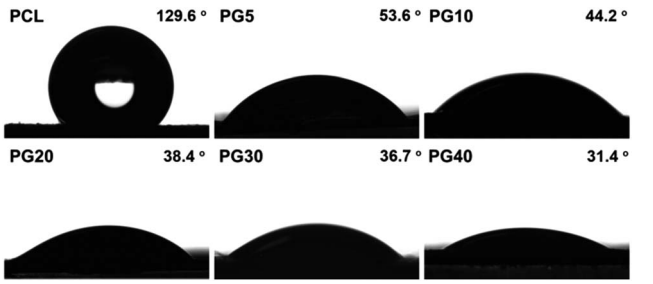

Fig. 3 Variation of the contact angle of the membrane with MNA content.

Published on 05 September 2014. Downloaded by Oregon State University on 6/23/2023 8:02:32 PM.

imidazole ring functional groups on the MNA molecule. Such an improvement in hydrophilicity will increase tissue regeneration and the biodegradation rate of the membranes.

3.1.4 Drug encapsulation efficiency and drug release profile. Drug encapsulation efficiency is highly influenced by the solubility and compatibility of the drug and polymer matrix with each other in the electrospun solution. The drug encapsulation efficiencies of the membranes are summarized in Table 2. All the membranes have high drug encapsulation efficiencies (above 80%) because of the good dispersion of MNA in the fibers and the interaction between MNA and the polymer matrix. With the increase of drug loading, the drug encapsulation efficiency decreases, probably because of the loss of a small part of the aggregated drug that cannot be encapsulated into the fibers.

The drug release profiles of the membranes are presented in Fig. 4. The sink condition during the experiment was maintained according to the calculation and dissolution curve as shown in S8† to make sure the realistic of the drug release study. About 40–50% of MNA is released from the membranes within 1 day, with an initial burst release. After the initial burst release, the MNA tends to release at a slower rate in the following 6 days. During the first week, gelatin nanofibers degraded, while PCL did not. The mechanism of drug release was based on drug diffusion and gelatin biodegradation. The interaction between MNA and gelatin and the HBs between MNA and PCL led to a sustained release of MNA from the fibers. The smaller the diameter of the fibers, the shorter the drug diffusion route and the faster the drug release. The drug is distributed in the macro- and nanofibers separately, resulting in different drug release stages. The crystallinity of PCL also affected the drug release profile. Under the effects of these factors, the membranes show a controlled and sustained drug release. The drug release periods of the membranes are efficiently anti-infective because the first week after the GTR/GBR membrane implanted into a tissue defect site is the high-incidence season of infection and inflammation.

Table 2 Drug encapsulation efficiency of the PG–MNA membranes

Sample	PG5	PG10	PG20	PG30	PG40
Drug encapsulation efficiency/%	92.4	90.7	87.5	84.9	84.1

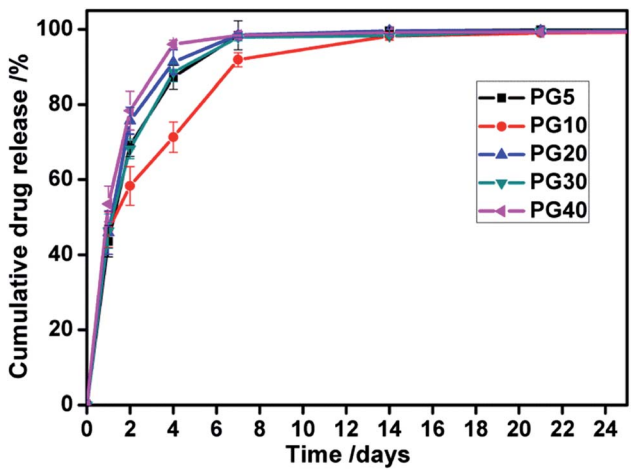

Fig. 4 Cumulative drug release profiles of electrospun PG–MNA membranes at different soaking times in PBS.

3.1.5 *In vitro* biodegradation of PG–MNA membranes. The mass loss curves of different electrospun membranes are shown in Fig. 5(a). In the first week, the mass loss of P30 is mainly due to MNA release while the mass loss of PG30 is much higher than that of P30 because of the degradation of gelatin. Gelatin takes only a few days to completely dissolve in water. The dramatic mass loss in the 7 days is caused by both drug release and gelatin hydrolysis and is followed by a slow, linear degradation caused by the slow hydrolysis of PCL molecules. After degradation for 3 months, 50% mass of PG–MNA membranes still remain.

As shown in the SEM micrographs of the membranes after degradation for 1 month, the gelatin nanofibers have disappeared, and microcracks are observed on the surfaces of the PCL microfibers; that is, the fiber surfaces have become rough. As indicated in Fig. 5(b), after degradation for 1 month, the tensile strength for each membrane is sufficiently high to support the growth of new tissues, and the elongation at break increases with the degradation of gelatin. With the incorporation of gelatin, the biodegradation rate of the membrane is accelerated.

3.2 *In vitro* biocompatibility and antibacterial property of PG–MNA membranes

3.2.1 *In vitro* antibacterial activity of PG–MNA membranes. Bacterial inhibition experiments were used to determine the minimal inhibition content of MNA loaded in the membranes. The growth of *Fusobacterium nucleatum* can be visualized directly from the plate (Fig. 6) to assess the antibacterial activity. No antibacterial activity is detected for PG0 at any time. In contrast, bacterial inhibition zones are clearly observed on the MNA-loaded membranes, and the inhibition area increases with the increase of MNA content. The MNA-loaded membranes can maintain the long-term antibacterial effects because of the slow but sustained release of MNA. Additionally, the released drugs can inhibit bacterial growth in an area much larger than the membrane size because of the diffusion of the drug into the agar.

3.2.2 Cytotoxicity. The results of the *in vitro* cytotoxicity (see S9†) reflect that all membranes show no cytotoxicity. L929 cells show health growing morphologies incubated in the extract substrates of the membranes. The membranes also show no cytotoxicity to hPDLFs and ROS cells.

3.2.3 Attachment and proliferation of cells on PG–MNA membranes. Attachment, adhesion, and spreading occur in the first phase of cell–material interactions and will influence the cell's capacity to proliferate on the biomaterial and cell morphology. Generally, hydrophobic surfaces lead to lower cell adhesion than hydrophilic surfaces. The optical density

 This journal is © The Royal Society of Chemistry 2014

Published on 05 September 2014. Downloaded by Oregon State University on 6/23/2023 8:02:32 PM.

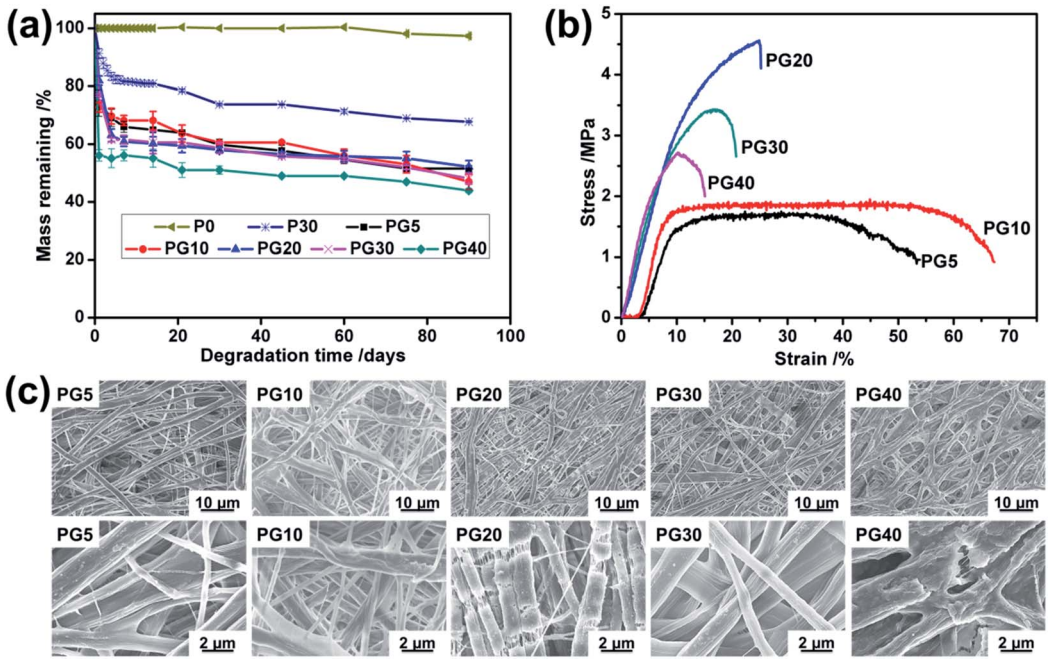

Fig. 5 *In vitro* degradation of electrospun membranes: (a) mass loss during 3 months degradation, and (b) stress–strain curves and (c) SEM micrographs of membranes after degradation for 1 month in PBS.

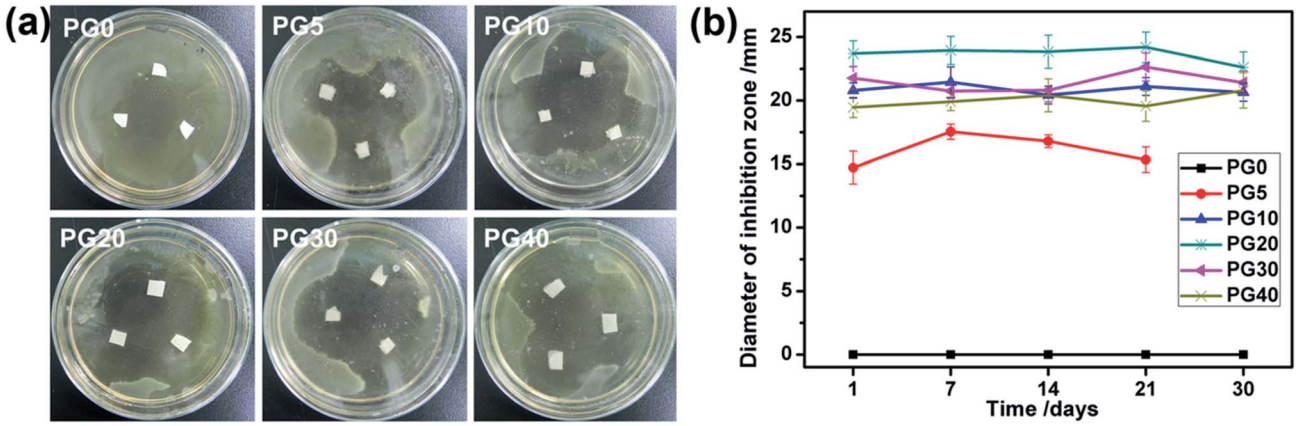

Fig. 6 Inhibition of bacterial growth on agar plates: (a) inhibition zone surrounding membranes with different contents of drug after incubation for 1 day under anaerobic conditions at 37 °C; (b) inhibition zone diameter *versus* incubation time for membranes with different MNA contents.

(O.D.) of L929 cells adhered to TCP (the control) and the membranes after being seeded for 4 hours are shown in Fig. 7(a). There are no significant statistical differences of the adhered cell number between the membranes with different MNA contents.

As shown in Fig. 7(b), for all the tested membranes, especially PG10, PG20 and PG30, with incubation, the number of cells increases continuously during the 7 days of culture, indicating that all the membranes are nontoxic. The cells grow better on the electrospun membranes than on TCP because of the mimic ECM structure of the electrospun membranes. The hydrophilicity of the membranes increases with increasing MNA content. The increased hydrophilicity is beneficial to the promotion of cell growth. The presence of micro- and nanofibers increases the surface roughness. The release of drug crystals on the surface of PG20, PG30, and PG40 increases the fiber surface roughness. Cells tend to proliferate on a rougher surface. For PG40, as the MNA released in the culture medium reach a sufficiently high content, the cell growth is adversely affected. So with the good hydrophilicity, increased surface roughness, and appropriate drug content, PG10, PG20 and PG30 show better *in vitro* biocompatibility than the other membranes. Besides, because the antibacterial activity increases with the MNA content, so 30 wt% MNA content is the highest drug content with the best antibacterial activity while without cytotoxicity.

Published on 05 September 2014. Downloaded by Oregon State University on 6/23/2023 8:02:32 PM.

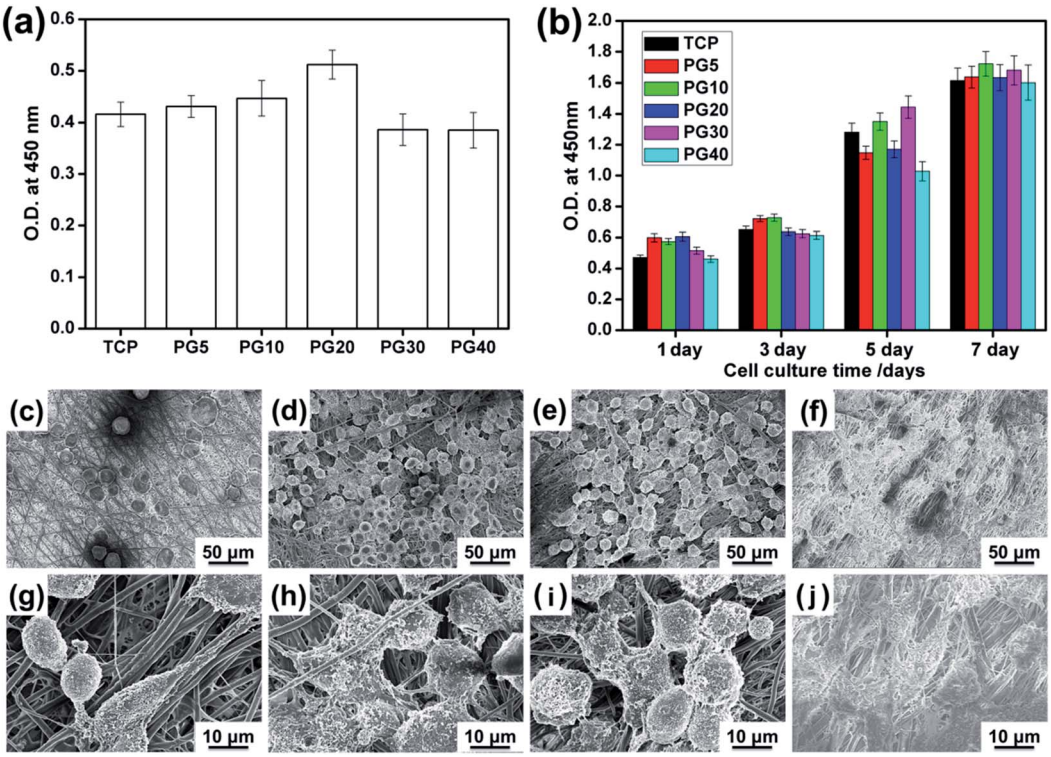

Fig. 7 The optical density (O.D.) of L929 cells (a) adhered for 4 hours and (b) proliferated for 1, 3, 5, and 7 days on the membranes tested by using CCK-8 assay. SEM micrographs of L929 fibroblasts proliferated on the PG30 membrane for (c) and (g) 1 day, (d) and (h) 3 days, (e) and (i) 5 days and (f) and (j) 7 days by SEM.

The morphology of L929 cells proliferating on PG30 was observed. The cells grow on the surface of the membrane without infiltrating in the thickness direction because of the small pore size of the membrane. With proliferation, the cells form almost a confluent layer with the characteristic spindle shape and stretch across the substrate on day 7. The specific structures related to the cell motility of fibroblasts—filopodia and lamellipodia—can be observed. The cells emit a cytoplasmic process towards the fibers and neighboring cells, communicating with the surrounding micro-environment and neighboring cells and allowing the passage of messengers.[32] Thus, we can conclude that even with a high content of drug and the use of organic solvent during the electrospinning process, PG30 has no negative effect on cell morphology, viability, and proliferation. As shown in Fig. 8, hPDLFs and ROS cells also proliferate well after incubation for 48 hours on PG30, with no statistical difference compared with cells proliferating on TCP as blank control.

3.2.4 Barrier function to fibroblast cells. One function of the GTR membrane is to prevent the ingrowth of fibroblast cells into the tissue defect site. We designed a novel method to test the barrier function of the membranes *in vitro*. No cells penetrate to the opposite side of the membrane from Fig. S7,† because the pores formed in the nanofiber membrane are much smaller than the fibroblast cells. After degradation for 1 month, all the membranes can still prevent the fibroblast cells from growing into them.

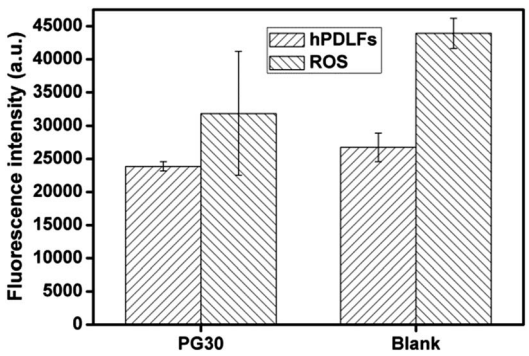

Fig. 8 Fluorescence intensity of hPDLFs and ROS cells cultured on PG30 for 48 hours.

3.3 *In vivo* biocompatibility and degradation of membranes

3.3.1 Gross morphology. The long term biocompatibility and biodegradation properties of PG30 were compared with those of P0 and P30 by subcutaneous implantation for 6 months. During the experiment, all rabbits remained in good health with no wound complications. For all membranes, no acute or chronic inflammation, necrosis, or adverse tissue reaction were identified. PG30 was absorbed completely after 6 months.

3.3.2 Histology. Host reactions following implantation of biomaterials include injury, blood–material interactions, provisional matrix formation, acute inflammation, chronic

 This journal is © The Royal Society of Chemistry 2014

Published on 05 September 2014. Downloaded by Oregon State University on 6/23/2023 8:02:32 PM.

inflammation, granulation tissue development, foreign body reaction, and fibrous capsule development.[34] At 1 week post-operation, the acute inflammatory response to biomaterials, marked by the presence of neutrophils, usually resolves quickly. As shown in Fig. 9, at 1 week implantation, no neutrophils are observed for P0, P30, and PG30, an indication of no obvious inflammatory response for these membranes. Cell infiltration on PG30 and P30 is, on average, less than that on P0 after 1 week. Following acute inflammation, chronic inflammation is identified by the presence of mononuclear cells at the implant site. There are more mononuclear cells around P0 and P30 than around PG30 at 3 weeks implantation. The acute and chronic inflammatory responses last no longer than 3 weeks, showing that the membranes are all biocompatible.

The number of macrophages around the samples is in the order P0 > P30 > PG30, and PG30 and P30 induce the formation of a much thinner inflammatory fibrous capsule than P0 after 3 and 8 weeks implantation. The formation of thick capsules is taken as an indication of poor biocompatibility. At 8 weeks implantation, fibroblasts have infiltrated into the inside of PG30, and the surrounding tissue shows a normal wound healing process, while no fibroblast has infiltrated into P0 and P30 because the degradation of gelatin accelerates the biodegradation of PG30. At 12 weeks implantation, a mass of fibroblasts and blood vessels are observed in the inner part of PG30, most part of which is replaced by a fibrous tissue and the barrier function disappears. Integration of the membrane and tissue at the interface is achieved. At 24 weeks, PG30 is completely absorbed and replaced by normal tissue without any infection or inflammation.

3.3.3 ***In vivo*** **degradation.** In the design of the GTR/GBR membrane, it is important to match the *in vivo* degradation rate of the membrane with the tissue regeneration rate.[31] The morphological changes of the nanofibers during *in vivo* degradation were evaluated by observing cross-sections of the membranes by SEM (Fig. 10(b)).

Both P0 and P30 degraded after 12 weeks, but did not show obvious fragmentation after implantation. For PG30, the gelatin nanofibers degraded only 1 week implantation, increasing the degradation rate of the PCL microfibers and the membrane. After 24 weeks, PG30 was absorbed and replaced by collagen and new formed tissue.

The *in vivo* experiments demonstrated that the organic solvent used in the electrospinning process had no adverse effect on the biocompatibility of the membranes. The membranes had good barrier function, as shown by the *in vitro* experiments, which could be used to effectively predict the *in vivo* barrier function of the membranes. Thus, some animal experiments could be avoided. With the incorporation of MNA and gelatin, PG30 was effective in reducing the inflammatory response after implantation and showing a more favourable tissue response profile and better biocompatibility. The biodegradation rate was appropriate for GTR/GBR membranes. This antibacterial drug-loaded membrane containing micro-

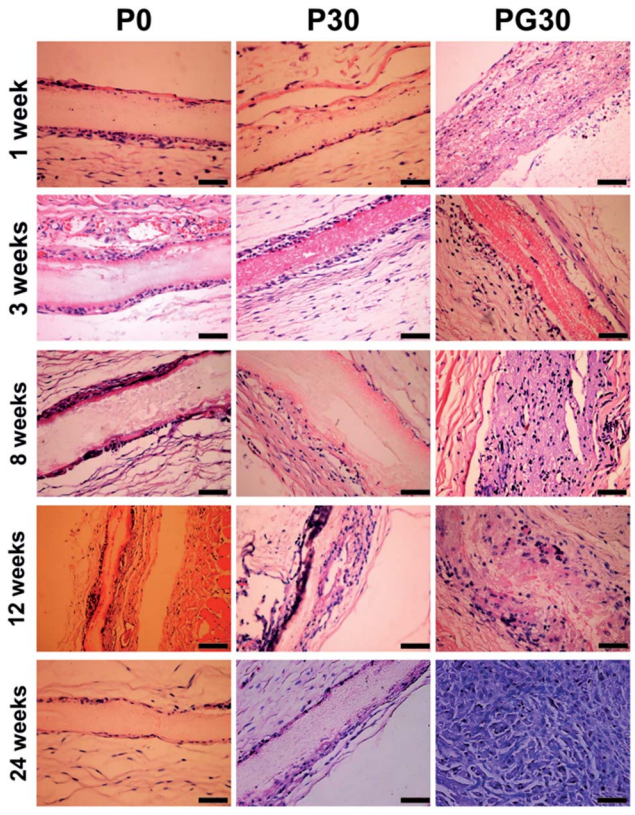

Fig. 9 Histological micrographs of P0, P30 and PG30 with H&E staining (scale bar = 100 μm).

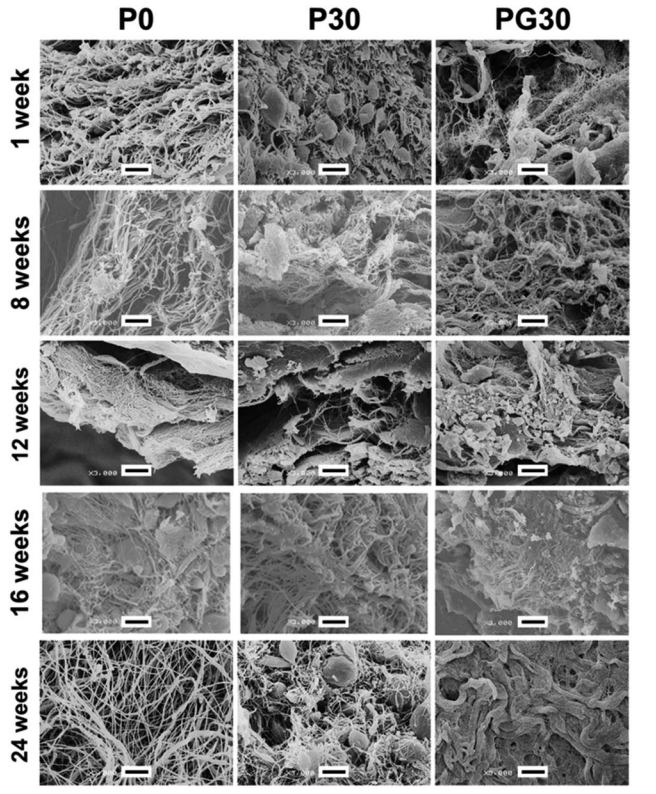

Fig. 10 SEM micrographs of longitudinal sections of membranes at different times after subcutaneous implantation (scale bar = 5 μm).

Published on 05 September 2014. Downloaded by Oregon State University on 6/23/2023 8:02:32 PM.

and nano-fibers can be used as an efficient GTR/GBR membrane.

4 Conclusions

We developed an efficient, anti-infective GTR/GBR membrane made by metronidazole-loaded electrospun PCL–gelatin micro-/nanofibers. A wide range of drug contents (1–40 wt%) were successfully incorporated into and released from the membranes. The properties of the membranes were found to be dependent on the drug content. The membranes were capable of effectively delivering MNA in a controlled manner and inhibiting anaerobic bacterial growth. Cells could adhere to and proliferate on the membranes. The incorporation of gelatin increases the biocompatibility and the biodegradation rate of the membranes. PG30 showed excellent comprehensive properties *in vitro*. The controlled release of MNA from PG30 can reduce the inflammatory response of the membrane upon implantation in rabbits by delivering MNA locally. Hence, PG30 could be an optimal choice for the localized drug delivery GTR/GBR membrane for the prevention of implant-associated infection. Besides, this drug delivery membrane can be used in various therapeutic applications in which controlled drug delivery is necessary, including pathologies demanding chronic drug treatments, wound healing, prevention of post-surgical adhesions and tissue engineering applications.

Acknowledgements

This work was supported by the National Natural Science Foundation of China (50933001, 51221102, 51303014), the National Outstanding Youth Science Fund (50725310), the National Basic Research Program (973 Program) of China (2011 CB606003), the Beijing Nova Program (Z131102000413015), the Beijing Municipal Training Programme Foundation for the Talents (2013D00303400041), and the RCUK China-UK Science Bridges Program through the Medical Research Council and the Engineering and Physical Sciences Research Council.

Notes and references

1 T. Karring, S. Nyman and J. Lindhe, *J. Clin. Periodontol.*, 1980, **7**, 96–105.
2 M. C. Bottino, V. Thomas, G. Schmidt, Y. K. Vohra, T.-M. G. Chu, M. J. Kowolik and G. M. Janowski, *Dent. Mater.*, 2012, **28**, 703–721.
3 K. Vasilev, J. Cook and H. J. Griesser, *Expert Rev. Med. Devices*, 2009, **6**, 553–567.
4 S. Sowmya, J. D. Bumgardener, K. P. Chennazhi, S. V. Nair and R. Jayakumar, *Prog. Polym. Sci.*, 2013, **38**, 1748–1772.
5 D. Campoccia, L. Montanaro and C. R. Arciola, *Biomaterials*, 2013, **34**, 8533–8554.
6 D. Campoccia, L. Montanaro and C. R. Arciola, *Biomaterials*, 2013, **34**, 8018–8029.
7 S. Xin, X. Li, R. Huang, X. Xu, Z. Lei and H. Deng, *J. Biomed. Nanotechnol.*, 2014, **10**, 803–810.
8 K. Feng, H. Sun, M. A. Bradley, E. J. Dupler, W. V. Giannobile and P. X. Ma, *J. Controlled Release*, 2010, **146**, 363–369.
9 N. M. Vacanti, H. Cheng, P. S. Hill, J. O. D. Guerreiro, T. T. Dang, M. Ma, S. E. Watson, N. S. Hwang, R. Langer and D. G. Anderson, *Biomacromolecules*, 2012, **13**, 3031–3038.
10 K. Qiu, C. He, W. Feng, W. Wang, X. Zhou, Z. Yin, L. Chen, H. Wang and X. Mo, *J. Mater. Chem. B*, 2013, **1**, 4601–4611.
11 H. Xu, H. Li and J. Chang, *J. Mater. Chem. B*, 2013, **1**, 4182–4188.
12 W. Li, X. Li, Q. Wang, Y. Pan, T. Wang, H. Wang, R. Song and H. Deng, *Carbohydr. Polym.*, 2014, **99**, 218–225.
13 J. Zeng, L. Yang, Q. Liang, X. Zhang, H. Guan, X. Xu, X. Chen and X. Jing, *J. Controlled Release*, 2005, **105**, 43–51.
14 Q. Wang, N. Zhang, X. Hu, J. Yang and Y. Du, *J. Biomed. Mater. Res., Part A*, 2007, **82**, 122–128.
15 K. J. Shields, M. J. Beckman, G. L. Bowlin and J. S. Wayne, *Tissue Eng.*, 2004, **10**, 1510–1517.
16 J. Bergsma, W. De Bruijn, F. Rozema, R. Bos and G. Boering, *Biomaterials*, 1995, **16**, 25–31.
17 M. A. Woodruff and D. W. Hutmacher, *Prog. Polym. Sci.*, 2010, **35**, 1217–1256.
18 T. K. Dash and V. B. Konkimalla, *J. Controlled Release*, 2012, **158**, 15–33.
19 Z. Ma, W. He, T. Yong and S. Ramakrishna, *Tissue Eng.*, 2005, **11**, 1149–1158.
20 D. Gupta, J. Venugopal, M. P. Prabhakaran, V. Dev, S. Low, A. T. Choon and S. Ramakrishna, *Acta Biomater.*, 2009, **5**, 2560–2569.
21 J. Xue, B. Feng, R. Zheng, Y. Lu, G. Zhou, W. Liu, Y. Cao, Y. Zhang and W. J. Zhang, *Biomaterials*, 2013, **34**, 2624–2631.
22 R. Zheng, H. Duan, J. Xue, Y. Liu, B. Feng, S. Zhao, Y. Zhu, Y. Liu, A. He and W. Zhang, *Biomaterials*, 2014, **35**, 152–164.
23 E. Chong, T. Phan, I. Lim, Y. Zhang, B. Bay, S. Ramakrishna and C. Lim, *Acta Biomater.*, 2007, **3**, 321–330.
24 D. Kai, M. P. Prabhakaran, G. Jin and S. Ramakrishna, *J. Biomed. Mater. Res., Part B*, 2011, **98**, 379–386.
25 M. S. Kim, I. Jun, Y. M. Shin, W. Jang, S. I. Kim and H. Shin, *Macromol. Biosci.*, 2010, **10**, 91–100.
26 S. Gautam, A. K. Dinda and N. C. Mishra, *Mater. Sci. Eng., C*, 2013, **33**, 1228–1235.
27 X. Yang, F. Yang, X. F. Walboomers, Z. Bian, M. Fan and J. A. Jansen, *J. Biomed. Mater. Res., Part A*, 2010, **93**, 247–257.
28 S. Löfmark, C. Edlund and C. E. Nord, *Clin. Infect. Dis.*, 2010, **50**, S16–S23.
29 M. Reise, R. Wyrwa, U. Müller, M. Zylinski, A. Völpel, M. Schnabelrauch, A. Berg, K. D. Jandt, D. C. Watts and B. W. Sigusch, *Dent. Mater.*, 2012, **28**, 179–188.
30 B. Kurtis, B. Ünsal, D. Çetiner, E. Gültekin, G. Özcan, N. Çelebi and Ö. Ocak, *J. Periodontol.*, 2002, **73**, 694–700.
31 D. J. Phillips, S. R. Pygall, V. B. Cooper and J. C. Mann, *J. Pharm. Pharmacol.*, 2012, **64**, 1549–1559.
32 R. Thakur, C. Florek, J. Kohn and B. Michniak, *Int. J. Pharm.*, 2008, **364**, 87–93.
33 W. Ji, F. Yang, H. Seyednejad, Z. Chen, W. E. Hennink, J. M. Anderson, J. J. van den Beucken and J. A. Jansen, *Biomaterials*, 2012, **33**, 6604–6614.

 This journal is © The Royal Society of Chemistry 2014

34 J. M. Anderson, A. Rodriguez and D. T. Chang, *Semin. Immunol.*, 2008, **20**, 86–100.
35 Y. Zhang, H. Ouyang, C. T. Lim, S. Ramakrishna and Z. M. Huang, *J. Biomed. Mater. Res., Part B*, 2005, **72**, 156–165.
36 J. Deitzel, J. Kleinmeyer, D. Harris and N. Beck Tan, *Polymer*, 2001, **42**, 261–272.
37 Q. P. Pham, U. Sharma and A. G. Mikos, *Biomacromolecules*, 2006, **7**, 2796–2805.
38 C. S. Ki, D. H. Baek, K. D. Gang, K. H. Lee, I. C. Um and Y. H. Park, *Polymer*, 2005, **46**, 5094–5102.

Published on 05 September 2014. Downloaded by Oregon State University on 6/23/2023 8:02:32 PM.